Identifying ultrasonic scattering sites from three-dimensional impedance maps

Jonathan Mamou and Michael L. Oelze
Bioacoustics Research Laboratory, Department of Electrical and Computer Engineering, University of Illinois, 405 North Mathews, Urbana, Illinois 61801

William D. O'Brien, Jr.[a)]
Bioacoustics Research Laboratory, Department of Electrical and Computer Engineering, University of Illinois, 405 North Mathews, Urbana, Illinois 61801and Department of Bioengineering, University of Illinois, 1406 West Green Street, Urbana, Illinois 61801

James F. Zachary
Department of Bioengineering, University of Illinois, 1406 West Green Street, Urbana, Illinois 61801 and Department of Veterinary Pathobiology, University of Illinois, 2001 South Lincoln, Urbana, Illinois 61802

(Received 4 March 2004; revised 30 August 2004; accepted 4 September 2004)

Ultrasonic backscattered signals contain frequency-dependent information that is usually discarded to produce conventional *B*-mode images. It is hypothesized that parametrization of the quantitative ultrasound frequency-dependent information (i.e., estimating scatterer size and acoustic concentration) may be related to discrete scattering anatomic structures in tissues. Thus, an estimation technique is proposed to extract scatterer size and acoustic concentration from the power spectrum derived from a three-dimensional impedance map (3DZM) of a tissue volume. The 3DZM can be viewed as a computational phantom and is produced from a 3D histologic data set. The 3D histologic data set is constructed from tissue sections that have been appropriately stained to highlight specific tissue features. These tissue features are assigned acoustic impedance values to yield a 3DZM. From the power spectrum, scatterer size and acoustic concentration estimates were obtained by optimization. The 3DZM technique was validated by simulations that showed relative errors of less than 3% for all estimated parameters. Estimates using the 3DZM technique were obtained and compared against published ultrasonically derived estimates for two mammary tumors, a rat fibroadenoma and a 4T1 mouse mammary carcinoma. For both tumors, the relative difference between ultrasonic and 3DZM estimates was less than 10% for the average scatterer size. [DOI: 10.1121/1.1810191]

PACS numbers: 43.80.Qf, 43.20.Fn, 43.80.Vj [FD] Pages: 413–423

I. INTRODUCTION

Conventional *B*-mode images are derived from backscattered radio frequency (rf) echo signals. The rf echoes are created by reflections from interfaces between acoustically different regions (macrostructure) and by coherent and incoherent scattering from tissue microstructures. Those echo signals contain frequency-dependent information about the smaller scale tissue structures (<wavelength). *B*-mode image processing removes the frequency-dependent information available in the rf echo signals. *B*-mode images are good at displaying larger scale tissue structures (>wavelength) but, to display and quantify smaller scale structures, the frequency-dependent information must be utilized.

The rf echo signals backscattered from biological tissues contain information about the size, shape, number, and relative impedance (ratio of the acoustic impedance difference between the background and the scatterers to that of the background, the acoustic impedance is defined as the product of the density and the speed of propagation of sound) of the scattering objects. The backscattered signal is a superposition of wavelets scattered from numerous small structures confined within the volume of ensonified tissue. The frequency-dependent backscattered signal is dependent on the average tissue properties (size, shape, number, compressibility, density) of the scatterers within the ensonified region relative to the compressibility and density of the medium surrounding the scatterers.[1] The backscattered signal is, therefore, modeled as a statistical distribution of scatterers.

It is hypothesized that enhancing existing *B*-mode images with quantified physical properties of the average tissue microstructures can improve diagnosis of diseased tissue. Quantitative ultrasound (QUS) images, images enhanced by scatterer parameters like the average scatterer size and acoustic concentration (product of the number density and the square of the relative acoustic impedance of the scatterers), have successfully been used to characterize different aspects of tissue microstructures. Noteworthy are the pioneering works that have demonstrated theoretically and experimentally the ability to ultrasonically quantify ocular, liver, prostate, renal, and cardiac tissues.[2–5] Research revealed[6] that the effective scatterer size in ocular tumors was a strong indicator of cancer. Further, QUS results have provided greater diagnostic accuracy in prostate cancer detection and lesion

[a)]Author to whom correspondence should be addressed; electronic mail: wdo@uiuc.edu

localization than all other noninvasive techniques combined.[7,8] Anisotropy measurements of renal tissues showed that changes in the scatterer strength (acoustic concentration) were responsible for the anisotropy of backscatter rather than changes in scatterer size.[5] QUS imaging techniques were shown to be capable of differentiating among conditions that caused increased cortical echogenicity and structural changes like glomerular hypertrophy.[9–12] Furthermore, QUS measurements agreed well with measurements of those structures in biopsy samples.

Recently, we examined two different types of tumors to determine if it were feasible to distinguish between the tumors and normal tissues based on scatterer property estimates.[13–15] In the first study, QUS images of spontaneous rat mammary tumors [fibroadenomas (Harlan, Indianapolis, IN)] and surrounding tissues were constructed and compared. In the second study, a carcinoma cell line [4T1 mouse mammary carcinoma, CRL-2539 American Type Culture Collection (ATCC, Manassas, VA)] was cultured and implanted into mice. Estimates of scatterer size and acoustic concentration were made for the fibroadenoma and were compared with the carcinoma estimates. A statistically significant difference between scatterer diameter estimates inside and outside the fibroadenomas was observed for five of the eight rats [analysis of variance (ANOVA), $p<0.05$].[16] A statistically significant difference between acoustic concentration estimates inside and outside the fibroadenomas was seen for all but one rat (ANOVA, $p<0.05$).[16] A clear distinction was seen between the two tumor types and between the surrounding normal tissues using a multivariate classification scheme.[15]

Even though the QUS images (scatter size and acoustic concentration) have shown their effectiveness in differentiating masses in animal mammary tumor models, what is missing to more fully exploit the QUS approach is an understanding of the anatomical scattering sources. This understanding is hypothesized to lead to the identification of the actual anatomical scattering sites in tissues. Identification of scatterering sites will lead to improved scattering models. These improved models will yield more accurate and precise parameter estimation techniques from which it is also hypothesized to lead to QUS capabilities for diagnosing disease. Identification of the scattering sites is also important for estimating the optimal frequency range of interrogation for different kinds of tissues. A very similar approach has been shown to be successful in the case of trabecular bones,[17] where a binary 3DZM was used to describe bone microstructures.

To accomplish these challenges, this contribution introduces a novel approach to identify the anatomical scattering sources. The approach uses volume sections (3D histologic maps) corresponding to actual scanned tumor volumes to generate a 3D impedance map (3DZM). The 3DZMs are created by manually aligning serial photomicrographs of tumor sections. Impedance values are assigned to the different stained structures by the use of look-up tables of acoustical properties of the different tissue elements. The Fourier transform of the 3D spatial autocorrelation function (SAF) of the 3DZM is then calculated and used to estimate scatterer properties.

II. THEORY

A. Weak scattering in an inhomogeneous medium

The theory of scattering of a propagating acoustic wave in a heterogeneous medium is reviewed.[18] Weak scattering is the case where the inhomogeneities that cause scattering have tissue property values (density, ρ, and compressibility, κ) very close to those of the rest of the medium. For an incident plane wave of unit amplitude, in the case of the Born approximation (multiple scattering is ignored), the backscattered pressure wave far from the interrogated (or scattering) volume is a spherical wave:

$$p_{\mathrm{bs}}=\frac{e^{-ikr}}{r}\Phi(2k), \tag{1}$$

where bs denotes backscattered, k is the propagation constant ($k=\omega/c$ where ω is the angular frequency and c is the propagation speed) and the angle distribution function, $\Phi(2k)$ is

$$\Phi(2k)=\frac{k^2}{4\pi}\int\int\int_{V_0}\gamma(r_0)e^{-2ikr_0}dv_0. \tag{2}$$

V_0 represents the scattering volume and the function $\gamma(r)$ is

$$\gamma(r)=\gamma_\kappa(r)-\gamma_\rho(r), \tag{3}$$

where

$$\gamma_\kappa(r)=\frac{\kappa(r)-\kappa_0}{\kappa_0} \tag{4}$$

and

$$\gamma_\rho(r)=\frac{\rho(r)-\rho_0}{\rho(r)}, \tag{5}$$

where $\rho(r)$ and $\kappa(r)$ are the density and compressibility of the scattering sites, and ρ_0 and κ_0 are the density and the compressibility of the material surrounding the scattering sites, respectively. $\gamma_\kappa(r)$ and $\gamma_\rho(r)$ are therefore the relative changes in compressibility and density in the scattering volume V_0, respectively.

The backscattered intensity is hence

$$I_{\mathrm{bs}}=Ak^4|\Phi(2k)|^2, \tag{6}$$

where A is a proportionality constant.

In the case of weak scattering, that is, when γ_κ and γ_ρ are very small (for example, <0.1 for this first-order Taylor series approximation to be accurate), the function $\gamma(r)$ approximates to[19]

$$\gamma(r)=-2\frac{z(r)-z_0}{z(r)}=-2\frac{\Delta z}{z}, \tag{7}$$

where z is the plane wave impedance $z=\rho c=\sqrt{\rho/\kappa}$, $z(r)$ is the acoustical impedance value at location r, and z_0 is the background impedance, that is, the impedance of the medium with no scatterers. Thus, the function $\gamma(r)$ is proportional to the relative change in acoustic impedance.

Combining Eqs. (2), (6), and (7) yields

$$I_{bs} = A' k^4 S(2k), \tag{8}$$

where

$$S(2k) = \left| \frac{\iiint_{V_0} (\Delta z/z)\, e^{-2ikr_0} dv_0}{\iiint_{V_0} (\Delta z/z)\, dv_0} \right|^2 = \frac{S'(2k)}{S'(0)} \tag{9}$$

and where A' is a new proportionality constant, and $S(2k)$ is normalized such that $S(0)=1$

The backscattered intensity divided by k^4 is proportional to the magnitude squared of the Fourier transform of the relative impedance function, which is equal to the Fourier transform of the SAF of the relative impedance function of the scattering volume.[20] $S'(2k)$ and $S(2k)$, defined by Eq. (9), are hence termed power spectrum and normalized power spectrum of the medium, respectively.

B. Form factor

Form factors (FFs) are functions that describe the amplitude of the backscattered intensity due to a single scattering structure as a function of frequency, or more commonly as a function of the wave vector amplitude k. The FFs are based on 3D spatial correlation models by assuming some form or shape for the scattering tissue structures. Usually simple scattering shapes are assumed and in most cases they have a spherical symmetry. Mathematically, FFs are related to the shape of the scatterer through the Fourier transform. Specifically, the FF is the Fourier transform of the 3D SAF of a 3D medium containing a single scatterer, that is, the magnitude squared of the Fourier transform of the single scatterer's shape. FFs are normalized to a value of 1 when $k=0$ and their derivative usually vanishes when $k=0$.[19] They are therefore readily comparable to the normalized power spectrum $S(2k)$ [Eq. (9)].

Commonly used FFs include the Gaussian, the fluid sphere, and the spherical shell. They all describe spherically symmetric scatterers and depend only on the radius a of the scattering structure. For the fluid sphere FF the scatterer is assumed to be a homogeneous sphere filled with a fluid. For the spherical shell FF the scatterer is assumed to be a solid shell and therefore no wave is propagated inside the sphere. The Gaussian FF is a continuous distribution with spherical symmetry of relative impedance between the scatterer and the surrounding medium. The common FF definitions are[1,19]

$$F_a^1(2k) = e^{-0.827k^2 a_{\text{eff}}^2} \quad \text{(Gaussian)}, \tag{10}$$

$$F_a^2(2k) = \left[\frac{j_1(2ka)}{(2/3)\, ka} \right]^2 \quad \text{(fluid sphere)}, \tag{11}$$

$$F_a^3(2k) = [j_0(2ka)]^2 \quad \text{(spherical shell)}. \tag{12}$$

The subscript eff in Eq. (10) denotes effective because the radius does not correspond to a sharp discontinuity for a continuous distribution; a_{eff} is related to the correlation distance, d, by $d=(3\sqrt{\pi/2})^{1/3} a_{\text{eff}} = 1.55 a_{\text{eff}}$.[19] The subscript eff is omitted in the remainder of the paper. Also, the term ''scatterer size'' will always refer to the diameter of the scatterer (i.e., $2a$ or $2a_{\text{eff}}$ for the Gaussian model). j_0 and j_1 are the spherical Bessel function of the first kind of order 0 and 1, respectively.

The Gaussian FF [Eq. (10)] has often been used to model scattering from soft tissues.[16,21,3] The Gaussian FF allows for efficient estimation schemes to be utilized when estimating scatterer properties, i.e., the scatterer size and acoustic concentration. Goodness-of-fit has been used to determine the best FF for describing scattering; however, the anatomical scattering sources are still undetermined. There may exist undiscovered FFs that better model scattering than those FFs commonly used. Faran has derived closed-form expressions for the scattering from cylinders and spheres[22] and Insana has compared common FFs [Eqs. (10)–(12)] with the results of the Faran theory for spheres.[1] Their results have shown variable agreement between closed-form results and the common FFs for different types of spherical scatterers. The variability is extremely dependent upon the acoustical properties of the considered spherical scattering structure being considered. Form factor models do not take into account the presence of shear waves in the scatterers, whereas the theory of Faran incorporates shear. Therefore, the FF models are expected to work well for soft tissue scattering that does not support significant shear wave.

III. METHODS

A. 3D impedance map

A 3D impedance map can be viewed as a computational phantom. It is essentially a 3D matrix that describes some of the acoustical properties of a tissue volume; the elements are the values of the acoustic impedance of the medium.

3DZMs are derived from a 3D histologic data set, and are independent of ultrasonically acquired and/or processed data. To produce a 3DZM, tissue is fixed in 10% neutral-buffered formalin, embedded in paraffin, sectioned, mounted on glass slides, and stained with H&E (Hematoxylin and Eosin stain). Hematoxylin stains negatively charged nucleic acids (chromatin in nuclei and ribosomes) blue. Eosin stains proteins pink such as cell cytoplasm, connective tissue, muscle, etc. Therefore, all cell structures with proteins stain pink and the more protein the darker the pink color.

Each stained section is photographed with a light microscope [Nikon (Nikon Corporation, Tokyo, Japan) Optiphot-2 optical microscope], the photographs digitized with a Sony (Sony Corporation, Tokyo, Japan) CCD-Iris/RGB color video camera as a bitmap image, and each bitmap image aligned (registered) to form the 3D histologic map. Structures of approximately 0.5 μm or larger can be resolved, therefore individual proteins and chromatin molecules cannot be resolved, but the organization of these molecules into tissue structure such as nuclei, chromatids, connective tissue, or muscle fibers allows them to be seen. Then, each bitmap image pixel value in the 3D histologic map is converted to an appropriate acoustic impedance value to form the 3DZM.

To convert each pixel value to an appropriate acoustic impedance value a color-threshold algorithm was used on every H&E stained bitmap image. The range of colors of the different structures in the bitmap images were recorded. Each structure was assigned an impedance value (Table I).

TABLE I. Impedance values used for the 3D impedance maps.

Rat fibroadenoma (Mrayl)	4T1 Mouse mammary carcinoma (Mrayl)
1.58—epithelial cells	1.45—fat
1.54—mammary duct	1.58—cytoplasm
	1.60—nuclei
	1.60—red blood cells
1.80—connective tissue (z_0)	1.80—connective tissue
	1.55—background (z_0)

The bitmap images represent a two-dimensional (2D) matrix with colors represented by three 8 bit values corresponding to red, green, and blue. The ranges of color values corresponding to the different structures were used to project the bitmap into a 2D matrix where certain color ranges, corresponding to identified structures, were given the value corresponding to its assigned impedance value from the table. Sometimes pixels in the bitmap images were of colors that did not correspond to identified color ranges. In the case of pixels outside the identified color ranges, nearest neighbor values were used to assign impedance values to the unidentified pixels.

Tissue proteins stained with eosin have shades of color ranging from very light pink to dark pink, depending on the concentration of protein within the structure. This differential staining allowed for the recognition of unique microstructures in the tissue. A range of colors corresponding to an identified microstructure in the stained bitmap images was then assigned a single color. The new single color was thus representative of the acoustic impedance for that tissue microstructure.

For each pixel of the same color in the color-thresholded bitmap image the same acoustic impedance value was assigned. Figure 1 shows an example of an original H&E stained photomicrograph of a tissue section and the color-thresholded bitmap from a rat fibroadenoma. The stained sections were manually registered. The number of tissue sections was kept at a reasonable number (66 maximum). However, increasing the number of tissue sections would result in the need for a registration algorithm to automatically align the sections because manually aligning the sections would become too labor intensive.

Two different mammary tumors were used in our analysis. The impedance values used for the different tissue microstructures contained in the tissue were somewhat empirical, but also based on a large body of measured data.[23–25] For most soft tissues, the propagation speeds and densities fall within a relatively narrow range (speeds: 1520–1580 m/s; densities: 980–1010 kg/m^3; impedances: 1.5–1.6 Mrayl), with whole blood (speed: 1580 m/s; density: 1040 kg/m^3; impedance: 1.6 Mrayl) at the high end of most soft tissues. For lipid-based tissues, both the speed and density are somewhat lower (speeds: 1400–1500 m/s; densities: 920–970 kg/m^3; impedances: 1.3–1.5 Mrayl). For the collagen-based tissues, both the speed and density are somewhat greater than most soft tissues (speeds: 1600–1700 m/s; densities: 1020–1100 kg/m^3; impedances: 1.6–1.9 Mrayl).

The first tumor was a rat fibroadenoma. Each of the 39 10-μm-thick tissue sections measured laterally 640 μm by 480 μm. Each bitmap image measured 800 pixels by 600 pixels. Thus, each pixel represents a square of size 0.8 μm by 0.8 μm. Figure 2(a) shows the 3D H&E stained histologic map. For this tumor, three impedance values were used (left column of Table I): 1.58 Mrayl [for the epithelial cells (in green in Fig. 2(a)], 1.54 Mrayl for the mammary duct (in red), and 1.8 Mrayl for the connective tissue (background impedance, z_0 in blue). The resulting 3DZM is displayed in Fig. 2(b).

The second tumor was a 4T1 mouse mammary carcinoma. Each of the 66 5-μm-thick tissue sections measured laterally 160 μm by 120 μm. Each bitmap image measured 800 pixels by 600 pixels. Thus, each pixel represents a square of size 0.2 μm by 0.2 μm. Figure 3(a) shows the 3D H&E stained histologic map.

For this tumor four distinct impedance values were used (right column of Table I): 1.45 Mrayl for the fat [white in Fig. 3(a)], 1.58 Mrayl for the cytoplasm (gray), 1.60 Mrayl for the nuclei (blue), 1.60 Mrayl for the red blood cells (red), and 1.8 Mrayl for the connective tissue (green). The resulting 3DZM is displayed in Fig. 3(b). Also, for this tumor the background impedance (z_0) was assumed to be 1.55 Mrayl.

All the 3D renderings [Figs. 2(a), (b), 3(a) and (b)] were obtained using the software package ETDIPS (www.cc.nih.gov/cip/software/etdips/; a multidimensional volume visualization and analysis software, co-developed by the US National Institutes of Health and the National University of Singapore).

B. Estimation technique

This section presents the methodology used to obtain estimates from the power spectrum of a 3DZM. First, the 3DZM is divided into smaller volumes called regions of interest (ROIs). By dividing the 3DZM into smaller volumes,

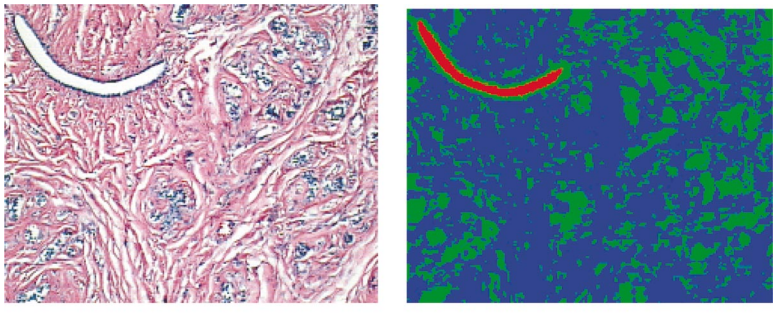

FIG. 1. The left image is a light microscopy illustration of the H&E-stained histology of a tissue section. The right image is the impedance map derived from this histologic section. Both images are 480 μm by 640 μm.

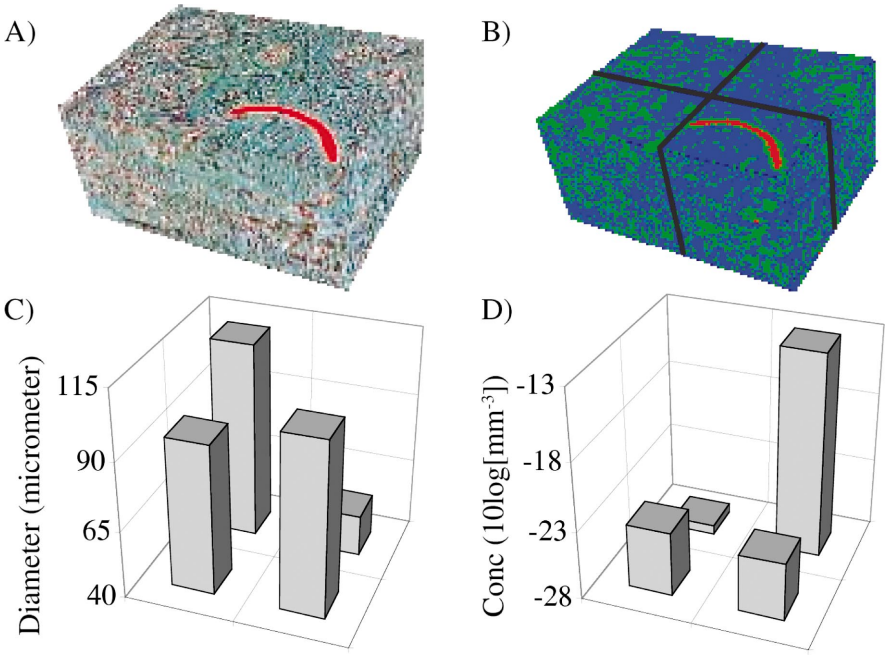

FIG. 2. (a) 3D H&E-stained histology of a fibroadenoma. (b) Derived 3D impedance map, black lines show the four ROIs. (c) Estimated scatterer diameter. (d) Estimated acoustic concentration. The volumes shown in (a) and (b) are of size 640 μm×480 μm×390 μm.

statistics about the estimates can be calculated from the different ROIs to show the precision of the estimation scheme. The scatterer size and acoustic concentration are then estimated for each ROI by an estimation routine that fits the Gaussian FF to the power spectrum. The Gaussian FF was used so that results obtained herein could be compared with published experimental ultrasound estimates[16] that used the Gaussian FF. However, the estimation technique could be used the same way with any FF. Estimates are obtained by minimizing the mean squared error between the log of the normalized power spectrum $[S(2k)$; Eq. (9)] and the log of the Gaussian FF [Eq. (10)] over the radius a, that is,

$$a^* = \operatorname{argmin}\left[\int_{k_{\min}}^{k_{\max}} [\log(S(2k)) - \log(F_a^1(2k))]^2 dk\right]. \tag{13}$$

The value of a that gives the smallest mean squared error is the scatterer radius estimate (a^*). Because the log of the Gaussian FF is $-0.827(ka)^2$, that is, a linear function of $(ka)^2$, the complexity of the minimization routine is reduced and allows for an efficient least squares solution.

However, it is not always possible to accurately obtain the normalized power spectrum $[S(2k)$; Eq. (9)] directly from the power spectrum $[S'(2k)$; Eq. (9)], because the

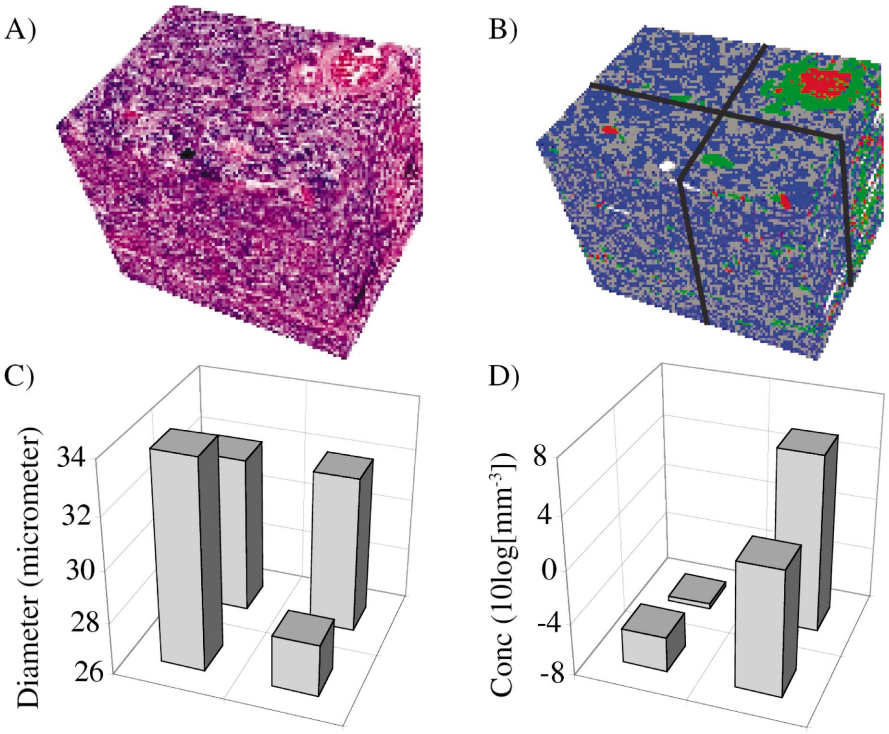

FIG. 3. (a) 3D H&E-stained histology of a 4T1 mouse mammary carcinoma. (b) Derived 3D impedance map, black lines show the four ROIs. (c) Estimated scatterer diameter. (d) Estimated acoustic concentration. The volumes shown in (a) and (b) are of size 160 μm×120 μm×330 μm.

computed $S'(0)$ might be very inaccurate. When $k=0$ the phase terms due to the random locations of scatterers add up instead of canceling each other as is the case when $k>0$. This fact makes the computed value of $S'(0)$ very different from its theoretical value [Eq. (9)]. Thus, Eq. (13) is slightly modified to include a gain parameter G_a, so that $S'(2k)$ can be used directly instead of $S(2k)$. The gain parameter G_a is obtained from

$$\log(G_a) = \sqrt{\frac{1}{k_{\max}-k_{\min}}\int_{k_{\min}}^{k_{\max}} |\log(S'(2k))-\log(F_a^1(2k))|^2 dk}. \tag{14}$$

Equation (14) is one of the choices to estimate a coefficient of proportionality between two functions. In particular in the idealistic case where S' and F_a^1 are proportional ($S'=\Gamma F_a^1$, where Γ is a proportionality constant), Eq. (14) yields $G_a=\Gamma$.

The gain parameter G_a is dependent upon a and can also be related to the acoustic concentration,

$$C=n\left[\frac{z-z_0}{z_0}\right]^2, \tag{15}$$

where n is the number density of scatterer, $(z-z_0)/z_0$ is the relative impedance mismatch between the scatterers and the background impedance, and z_0 is the background impedance. G_a and C are then related by

$$C=G_a/V_s^2, \tag{16}$$

where V_s is the volume of a single scatterer.[19] V_s is equal to $\frac{4}{3}\pi a^3$ for the fluid sphere and the spherical shell. V_s is also equal to $\frac{4}{3}\pi a^3$ for the Gaussian sphere.[1,19]

Incorporating the gain parameter G_a, Eq. (13) becomes

$$a^*=\text{argmin}\left[\int_{k_{\min}}^{k_{\max}}[\log(S'(2k))-\log(G_aF_a^1(2k))]^2 dk\right], \tag{17}$$

in which $S(2k)$ has also been replaced with $S'(2k)$. Equation (17) is now easier to solve because $S'(2k)$ is simple to compute from the 3DZM. $S'(2k)$ is the magnitude squared of the Fourier transform of the 3D impedance map. Also from a^*, we can compute G_{a^*} and therefore estimate the acoustic concentration C^* from Eq. (16).

In order to solve Eq. (17), it is necessary to properly select the optimization range, $k_{\min}$ and $k_{\max}$. An optimal ka^* range has been defined to be between 0.5 and 1.2 for the case of glass beads.[1] However, for the case of smoother FF (like the Gaussian FF) only the lower limit is the most important. For this work the ka range was chosen to be 0.5–2.0. For $ka^*<0.5$, FFs are usually flat (their derivative vanishes as ka^* approaches 0), which leads to large inaccuracies in the estimates: estimates are found to be close to the lower bound of the estimation range (usually below 3–5 μm). For $ka^*>2.0$, FF amplitudes are usually very low (e.g., -15 dB for the Gaussian FF) and noise can be dominant (backscattered signal amplitudes are already around -60 dB or less[1]). Table II shows the frequency ranges for scatterer of radii 10, 50, and 100 μm deduced from $ka=0.5$ and $ka=2.0$. A speed of sound of 1540 m/s was assumed.

TABLE II. Frequency ranges deduced from $ka=0.5$ and $ka=2.0$ ($c=1540$ m/s).

Scatterer radius (μm)	Frequency range (MHz)
10	12.3–49.0
50	2.45–9.80
100	1.23–4.90

The challenge for defining the optimal ka^* range is that it depends upon the estimated radius that is unknown. One approach could be to chose an average radius and then deduce from the optimal ka range values for $k_{\min}$ and $k_{\max}$. However, computational trials using this approach have shown a bias in the estimates: all estimates were found to be within a few percent of the average radius chosen.

An alternate approach was used to define $k_{\min}$ and $k_{\max}$. The goal of this approach was to obtain estimates that were not biased by the selected frequency range. Two new parameters k_{start} and Δk, were defined where $k_{\text{start}}=k_{\min}$ and $\Delta k=k_{\max}-k_{\min}$. An error function for the radius a is computed from

$$\text{Err}(a)=\text{Max}\{E(a,k_{\text{start}},\Delta k), \quad \text{for every } k_{\text{start}} \text{ and } \Delta k\}, \tag{18}$$

where

$$E(a,k_{\text{start}},\Delta k)=\frac{1}{\Delta k}\left[\int_{k_{\text{start}}}^{k_{\text{start}}+\Delta k}[\log(S'(2k)) - \log(G_aF_a^1(2k))]^2 dk\right], \tag{19}$$

and where the Err function is defined by the maximum of the mean squared errors over every frequency range. The optimal ka range is hence enforced by setting $E(a,k_{\text{start}},\Delta k)=0$ if $k_{\text{start}}a<0.5$ or $(k_{\text{start}}+\Delta k)a>2.0$.

Finally, a^* was defined as the argument of the absolute minimum of Err. This scheme has no built-in bias, because it evaluates every scatterer radius size over every frequency range while enforcing the optimal ka range. In particular, no specific frequency range has to be enforced. Thus, the strategy may possess the ability to find different populations of scatterers (different size, shape, impedance distribution, etc). Populations of scatterers may be revealed by determining the different local minima of the Err function.

An alternate choice of the Err function could be

$$\text{Err}'(a)=\text{Min}\{E(a,k_{\text{start}},\Delta k), \quad \text{for every } k_{\text{start}} \text{ and } \Delta k\}, \tag{20}$$

as replacement for Eq. (18) [also, enforcing optimal ka range would be accomplished by requiring $E(a,k_{\text{start}},\Delta k)\to\infty$ if $k_{\text{start}}a<0.5$ or $(k_{\text{start}}+\Delta k)a>2.0$]. However, applying Eq. (18) leads to better results because the Err$'$ functions curves are usually very flat and their minima are impossible to differentiate from noise. Err functions curves usually show steep minima that are clearly distinct from noise.

TABLE III. Simulation estimates.

	Medium A	Medium B
Diameter (% error)	41.1±2.9 μm (2.8%)	81.1±6.1 μm (1.4%)
Concentration (% error)	−14.28±1.1 dB (mm^{-3}) (2%)	−13.88±1.2 dB (mm^{-3}) (0.8%)

IV. RESULTS

Estimates for scatterer size and acoustic concentration were obtained for simulated 3DZMs, and from a rat fibroadenoma and a 4T1 mouse mammary carcinoma using the above-described estimation scheme. The simulated 3DZM studies are intended to assess the feasibility of the 3DZM approach for obtaining size and acoustic concentration estimates. In the simulated 3DZMs the quality of the estimates can be quantitatively assessed because the actual values are known.

A. Simulated media

1. Single population simulations

The first two simulated media were 3DZMs of the same size (256 μm by 256 μm by 256 μm) containing 15 fluid sphere-like scatterers of the same diameter. The scatterer diameters were 40 μm for medium A and 80 μm for medium B. The background had an impedance of 1.50 Mrayl and the spheres had an impedance of 1.51 Mrayl. The acoustic concentration was the same for both media (same number density of scatterer and same impedance difference between scatterer and background), that is,

$$C=\frac{15}{(256\times10^{-6})^3}\left[\frac{1.51-1.50}{1.50}\right]^2=0.0397\ \ \mathrm{mm}^{-3}.$$

Acoustic concentration values may have a large dynamic range from one ROI to another. Therefore, acoustic concentration is expressed as: $C_{\mathrm{dB}}=10\log(C)$ [and not $20\log(C)$, because C is directly related to the amplitude of the power spectrum and is hence a second-order quantity]. For the two simulated media $C_{\mathrm{dB}}=-14.01\,\mathrm{dB\,mm}^{-3}$. For the simulations, in Eq. (17), F_a^1 was replaced by the FF for a fluid sphere case F_a^2, and each voxel in the 3DZM was represented by a cube of side length 1 μm. Fluid spheres were used because the Gaussian model was more computationally intensive due to the infinite ''size'' of the Gaussian ''spheres.''

For both simulated media, the power spectra from 10 random realizations of the 3DZMs were averaged to limit the noise due to the spatial variations of the locations of the spheres. Fifty 10-realization spectra were computed for each media. From the 50 spectra, 50 size (diameter) and acoustic concentration estimates were obtained (Table III). For both media the average estimates were close to the actual values (relative errors less than 3% for all 4 average estimates). Log(Err) plots as a function of the scatterer diameter for realizations of media A and B showed that absolute minima were located very close to the actual scatterer diameters (Fig. 4), that is, 40.8 μm for medium A and 81.0 μm for medium B. The values of Err at the minima were also very close for media A and B curves [log(Err) values were around −1.8 for both curves]. Thus, the single population simulation studies validated the 3DZM methodology as a means to obtain accurate estimates.

Figure 4 shows that diameters between 20 and 160 μm were tested. Because the ka range chosen for optimization was 0.5–2.0, one can deduce that the optimization scheme evaluated any frequency range included in the interval (1.53–49.0 MHz).

Both curves (Fig. 4) showed sawtooth-like behavior for large scatterer diameters. Equation (18) should yield a smooth curve if an infinite number of frequency ranges were evaluated. However, because a finite number of frequency ranges were evaluated, the sawtooth-like behavior resulted. Also, the sawtooth-like behavior was more likely to occur for large scatterer diameters because fewer frequency ranges were available from which to select, and because enforcing the upper bound of the ka range limited the number of frequency ranges available for large a. This phenomenon could be removed artificially by low-pass filtering the error curves or by increasing the zero padding when computing the spectra so that more frequency ranges were available.

2. Two populations simulations

The next simulations evaluated the feasibility of identifying two population sizes of scatterers buried in a single medium. Seven media were simulated and the impedance mismatches were the same for both populations: 1.51 Mrayl for the spheres and 1.50 Mrayl for the background (Fig. 5). The acoustic concentration of the 40 μm scatterers was constant at $-14.01\,\mathrm{dB\,mm}^{-3}$ (same value as for media A and B). The acoustic concentrations of the 80 μm scatterers were (from top to bottom at the horizontal axis location of about 40 μm): −9.01, −14.01, −17.01, −20.01, −23.01, −26.01, and $-29.01\,\mathrm{dB\,mm}^{-3}$. These 7 media were the same size as

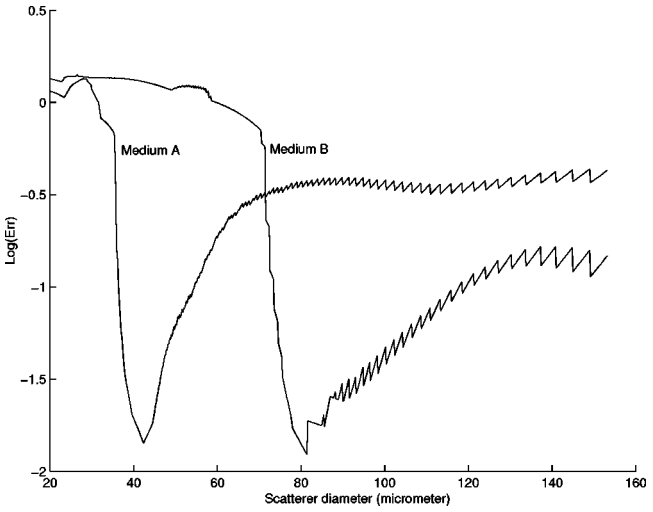

FIG. 4. Log(Err) vs scatterer diameter for realizations of media A and B.

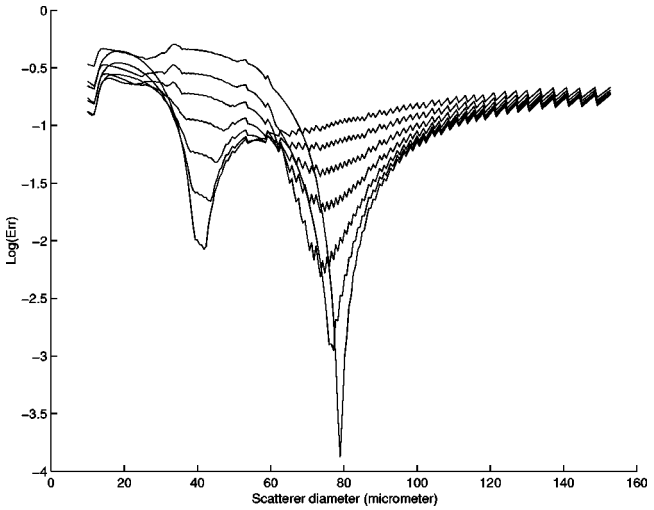

FIG. 5. Log(Err) vs scatterer diameter for realizations of two-population media. The acoustic concentration of the 40 μm scatterers was constant at -14.01 dB mm^{-3}. The acoustic concentrations of the 80 μm scatterers were (from top to bottom at the horizontal axis location of about 40 μm): -9.01, -14.01, -17.01, -20.01, -23.01, -26.01, and -29.01 dB mm^{-3}.

media A and B (cube with side length of 256 μm) and each voxel was represented by a cube of side length 1 μm.

As the acoustic concentration of the 80 μm scatterers increased, the topologies of the curves could be classified in three categories: (1) Single clear minimum around 40 μm (for 80 μm scatterer acoustic concentration of -29.01 and -26.01 dB mm^{-3}), (2) two clear minima around 40 μm and in the range 75–80 μm (for 80 μm scatterer acoustic concentration of -23.01 and -20.01 dB mm^{-3}), (3) single clear minimum near 80 μm (for 80 μm scatterer acoustic concentration of -17.01, -14.01, and -9.01 dB mm^{-3}). Hence, for the small scatterer population to be the only one detected [i.e., category (1)] a much higher acoustic concentration of small scatterers than large scatterers was necessary (a small scatterer acoustic concentration at least 12 dB mm^{-3} higher than that of the large scatterers). However, the large scatterer population is the only one detected [i.e., category (3)] when the small population acoustic concentration is at most 3 dB mm^{-3} higher than that of the large population. Finally, in between [i.e., category (2)], the curves tend to show two minima, one for each population.

A similar two-population study was also conducted where this time the number density was kept the same for the 40 and 80 μm populations. However, the impedance values of the 80 μm were varied. The impedance values chosen were such that the 80 μm acoustic concentration had the same seven values as in the previous simulations (-9.01, -14.01, -17.01, -20.01, -23.01, -26.01, and -29.01 dB mm^{-3}). Like before, the 40 μm acoustic concentration was kept at -14.01 dB mm^{-3}. The error curves obtained were extremely similar to those of Fig. 5.

These simulations showed that with a factor of 2 in size and under certain conditions (in particular concentration), it was possible to resolve the two populations using the 3DZM optimization scheme. However, it seems difficult to assess the resolution of the scheme based on this first set of two-population simulations.

The set of simulations showed that the 3DZM approach has the potential to resolve populations of different sized scatterers. Resolving different populations of scatterer size was possible only when the smaller sized scatterers' acoustic concentration was greater than that of the larger sized scatterers. The difficulty of resolving two scatterer size populations arises from the relative contribution of each population to the overall power spectrum. The power spectrum of a single population is proportional to Ca,[6] where a and C are the scatterer radius and acoustic concentration, respectively. Therefore, if the acoustic concentrations are equal, the contribution of the smaller sized scatterers to the overall magnitude of the power spectrum will be much less than the contribution of the larger sized scatterers because the spectrum is proportional to the radius to the sixth power.

These two 2-population studies demonstrated that the power spectrum is sensitive to the acoustic concentration, but not individually on the number density or the impedance values of the different scatterers. This is in accordance with ultrasonic scattering theory and was clearly pointed out by Insana.[1] Therefore, in order to resolve smaller scatterers in a two-population medium, either the number density of smaller scatterers must be much larger than that of the larger scatterers or the impedance mismatch for the smaller scatterers must be much larger than that for the larger scatterers.

B. Rat fibroadenoma results

The 3DZM of the rat fibroadenoma was divided into 4 ROIs, each of size 320 μm by 240 μm by 390 μm [Fig. 2(b)]. Figure 2(c) shows the scatterer size estimates and Fig. 2(d) shows the acoustic concentration estimates for the four ROIs. The mammary duct [in red in Fig. 2(b)] is present in two of the four ROIs, and appears in red in the bottom-right ROI. Also, the top-right ROI contains the mammary duct; however, it cannot be seen in Fig. 2(b) because it is not contained in the top section. The estimates obtained are very similar for the two ROIs that do not contain the mammary duct as well as the bottom-right ROI. However, the top-right size estimate is the smallest and the top-right concentration is the greatest. This might be due to the presence of the mammary duct. However, a similar effect was not observed in the estimates of the other ROI containing the mammary duct.

The error function (Fig. 6) contained a few distinct local minima (generally between one and three depending on the ROI). The estimates were obtained by selecting a minimum that was in the frequency range that was used for the same tumor when evaluated experimentally with ultrasound (-6 dB bandwidth 5–12 MHz).[16]

C. 4T1 mouse mammary carcinoma results

The 3DZM of the 4T1 mouse mammary carcinoma was divided into four ROIs, each of size 80 μm by 60 μm by 330 μm [Fig. 3(b)]. Figure 3(c) shows the scatterer size estimates and Fig. 3(d) shows the acoustic concentration estimates. The estimates are consistent among the four ROIs. However, the top-right ROI has the greatest acoustic concen-

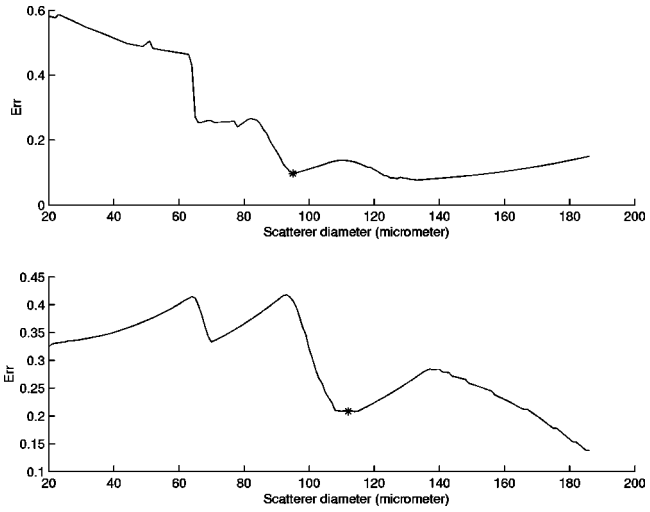

FIG. 6. Err function vs scatterer diameter obtained from two different ROIs of the rat fibroadenoma. Top curve was obtained from the top-left ROI of Fig. 2(b) and bottom curve was obtained from the top-right ROI of Fig. 2(b). The symbol "*" shows the selected minimum for each ROI.

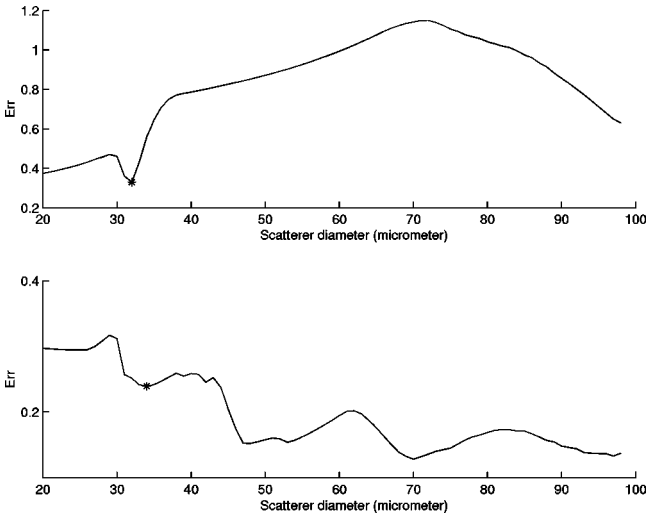

FIG. 7. Err function vs scatterer diameter obtained from two different ROIs of the 4T1 mouse mammary carcinoma. Top curve was obtained from the top-left ROI of Fig. 3(b) and the bottom curve was obtained from the bottom-left ROI of Fig. 3(b). The symbol "*" shows the selected minimum for each ROI.

tration (even though it does not have the smallest size estimate). This might be due to the presence of the red blood cells [in red in Fig. 3(b)] in this ROI.

Here also, the error function (Fig. 7) contained a few distinct local minima. The estimates were obtained by selecting a minimum that was in the frequency range that was used for the same tumor when evaluated experimentally with ultrasound (-6 dB bandwidth 10–25 MHz).[16] The top plot shows only one minimum, but the bottom plot shows four clear minima. However, for these two ROIs the selected size estimates were 32 and 34 μm, respectively.

D. Comparison with ultrasonic results

The estimates obtained using the 3DZM methodology for the two tumor types were compared to the published values obtained ultrasonically[14–16] (Table IV). The experimentally derived estimates represent a completely independent measure from that of the 3DZM estimates. The average scatterer size and acoustic concentration estimates (Table IV) were obtained by computing the mean and standard deviation of the estimates over the four ROIs for each of the two tumors. Results show a good agreement (difference less than 10%) for size estimates of both tumors. However, the acoustic concentration values are significantly different (difference greater than 6 dB mm^{-3}).

The 3DZM technique estimates of acoustic concentration were significantly smaller than those obtained ultrasonically (6.3 dB for the fibroadenoma and 11 dB for the 4T1 mouse mammary carcinoma). The difference in estimates might be due to several factors. First, more accurate impedance values may need to be assigned to a wider range of anatomic structures. In particular, a change in the background impedance value (z_0) will significantly modify the acoustic concentration estimates. Second, the internal distribution of acoustic properties (impedance) within the scattering structures will affect the estimates. Third, a small error in the estimate of the scatterer size can lead to a much larger error in the estimate of the acoustic concentration.[16] For example, a relative error of $+5\%$ of the scatterer size estimate will lead to a relative error of -27% of the acoustic concentration estimate.

It is encouraging that the scatterer size estimates obtained with the two independent techniques were directly comparable, because the scatterer size depends only on the variation of the power spectrum with frequency. However, the acoustic concentration depends upon the estimated scatterer size and the absolute amplitude values of the power spectrum.[16] The published acoustic concentration estimates determined ultrasonically were used only in a relative comparison. Absolute values for the acoustic concentration estimates were inaccurate because physical reflection losses (skin layer) were uncompensated. The physical reflection losses mostly change the absolute values of the power spectrum but not its variation with frequency. Therefore, acoustic concentration estimates found using the 3DZM may not be comparable to estimates obtained ultrasonically. The discrepancies between the ultrasonic and 3DZM acoustic

TABLE IV. 3D impedance map and ultrasound estimates.

	Rat fibroadenoma		4T1 mouse mammary carcinoma	
	Diameter (μm)	Concentration (dB mm^{-3})	Diameter (μm)	Concentration (dB mm^{-3})
Impedance map	91±25	−21.9±6.1	31.5±2.5	−1.4±6.1
Ultrasound	105±25	−15.6±5	30.0±9.6	10.6±6.9

concentration estimates need to be further investigated.

Some of the Err curves (Figs. 6 and 7) showed multiple local minima. The way the scatterer size estimate was selected among the multiple local minima was somewhat empirical. The minimum was selected in the frequency range that was used for the same tumor when evaluated ultrasonically and it is in part why the sizes agreed very well between the 3DZM and ultrasonic estimates. However, these Err curves (Figs. 6 and 7) all tended to have a local minima near the value found ultrasonically demonstrating agreement between the two independent techniques.

To assist with the understanding of the multiple local minima in the 3DZM-acquired curves, a next step would be to ultrasonically scan tissues over a wider range of frequencies, possibly with multiple transducers. Specifically, multiple minima may correspond to populations of scatterers with different sizes.

V. DISCUSSION

Identifying ultrasonic scattering sites would be a very beneficial adjunct to already existing QUS techniques. The work presented herein tackles this problem by using novel 3D representations of tissue microstructures (the 3DZM). In the present work, 3DZMs were used to obtain estimates of tissue microstructure parameters, namely the scatterer size and the acoustic concentration. The 3DZM estimation technique was shown to be very accurate for simulated 3DZMs (Table III). Estimates were also obtained for two mammary tumors and results were compared against published estimates that were obtained ultrasonically.[16] Average scatterer estimates for both techniques were within 10%. The results presented in this paper demonstrate that the 3DZMs may be accurate and useful representations of tissue microstructure. 3DZM approaches to ultrasonic scattering may hence have the potential to improve QUS techniques.

The methodologies presented herein characterize tissue microstructure from frequency-dependent information. The use of frequency-dependent scattering information from structures smaller than a wavelength has also been used to characterize different media using different energy sources. Laser scattering has been used to retrieve information about glass and polymer structures.[26] Neutron scattering has been used to measure molecular bond lengths.[27] Also, in acoustics, but in the low-frequency range (below 1 kHz), frequency-dependent scattering has been used to characterize turbules in the atmosphere.[28] Thus, ultrasonic scattering has been used[16,21,29] to quantitatively assess tissue microstructure. The 3DZM approach was developed to complement the ultrasonic estimation techniques, and further provide a computational tool for evaluating the anatomical scattering sites and sources.

The 3DZM approach is a powerful tool to obtain statistical descriptions of tissue microstructure. The 3DZM approach is a tissue-based capability to compute the power spectrum (and the spatial autocorrelation function, SAF) of the medium in a very straightforward way through the Fourier transform (see Sec. II A). To improve the power spectrum obtained from ultrasound, the ultrasonic techniques need to compensate for the experimental setting and the attenuation. Normalization removes dependence upon the experimental equipment[30] and attenuation compensation is used to mitigate the effects of attenuation.[31] If attenuation is not accounted for, estimates might become unreliable because attenuation is frequency dependent.

The power spectrum derived from ultrasonic measurements is only valid over the bandwidth of the transducer. Once the power spectrum is obtained, the optimization step in the ultrasonic technique is very similar to Eq. (13), except that $k_{\min}$ and $k_{\max}$ are fixed by the bandwidth of the transducer. The 3DZM approach has the advantage over the ultrasonic technique to obtain a power spectrum valid for a broader range of frequencies. The only limitation of the 3DZM approach is the absolute size of the tissue volume and the voxel size.

A couple of ways exist to improve the 3DZM technique. First, resolution could be improved. In particular, the section thickness could be reduced in order to have a similar pixel resolution in all three dimensions. Reducing the section thickness would also increase the similarities between two consecutive sections. Smaller slice thickness would have the advantage of being easier to align, or register, the sections.

Another improvement could be obtained by increasing the accuracy and the number of impedance values assigned to the different tissue structures. In some cases, it is difficult to measure acoustic properties of tissue microstructure, thus making the assignment of impedance values to different structures more challenging. However, an alternate technique might be used to deduce acoustic values by iteration. 3DZMs could be used as computational phantoms to simulate backscattered signals received by a given transducer. Then, comparison between simulation and ultrasonic experiments could be used to optimize the impedance values. At each step, the 3DZM would be updated until the simulated backscattered signals matched the signals obtained by ultrasonic measurements.

In the present work, the 3DZM methodologies were only conducted on tissues with lesions (i.e., tumors). Thus, the 3DZM methodology should also be tested on normal tissues to see whether the statistics of the 3DZM estimates would be different between healthy and diseased tissues. Estimates had different statistics on healthy and diseased tissues in the case of the ultrasonic techniques.[16]

The FF is, by definition, the normalized power spectrum of the 3DZM. Therefore, the 3DZMs can be used as a means to extract realistic FF through the Fourier transform. More interestingly, the 3DZM can also be used to help in identifying the anatomic scattering structures in tissues. From the inverse Fourier transform of the 3DZM-obtained FF, a 3D acoustic model of the SAF of a scattering structure can be determined. Then, it might be possible to identify the scattering sites by comparison of the SAF characteristics with the histology. Also, the assumed FF has great influence on the estimates. For example, the spherical shell FF has a steeper slope than that of the Gaussian FF.[1] Therefore, using the spherical shell FF would always lead to smaller estimates for the size and larger estimates for the acoustic concentration when compared to the estimates obtained with the Gaussian FF.

The spherical scattering assumption (or any nonspherical assumption) is still difficult to fully justify, because the scattering sites are unknown. It is our hope that the work provided in the manuscript can eventually lead to an understanding of the specific anatomic scattering sites which will then lead to a firm basis for the selection of a FF. Identifying the ultrasonic scattering sites would lead to great improvement of the diagnostic capabilities of quantitative ultrasound. Parameters could then be chosen that actually describe histology of tissue microstructures. Then, clinicians might be able to provide a diagnosis that is based on the ultrasonically obtained measurements of physical properties of tissue microstructure. Therefore, identifying the ultrasonic scattering sites may result in the possibility to develop novel and noninvasive diagnosis capabilities that are based on quantitative ultrasound approach.

ACKNOWLEDGMENT

The authors would like to acknowledge the support of the University of Illinois Research Board.

[1] M. F. Insana, R. F. Wagner, and D. G. Brown, ''Describing small-scale structure in random media using pulse-echo ultrasound,'' J. Acoust. Soc. Am. **87**, 179–192 (1990).
[2] J. E. Perez, J. G. Miller, B. Barzilai, S. Wickline, G. A. Mohr, K. Wear, Z. Vered, and B. E. Sobel, ''Quantitative characterization of myocardium with ultrasonic imaging,'' J. Nucl. Med. Allied Sci. **32**, 149–157 (1988).
[3] F. L. Lizzi, M. Greenebaum, E. J. Feleppa, M. Elbaum, and D. J. Coleman, ''Theoretical framework for spectrum analysis in ultrasonic tissue characterization,'' J. Acoust. Soc. Am. **73**, 1366–1373 (1983).
[4] F. L. Lizzi, M. Ostromogilsky, E. J. Felepa, M. C. Rorke, and M. M. Yaremko, ''Relationship of ultrasonic spectral parameters to features of tissue microstructure,'' IEEE Trans. Ultrason. Ferroelectr. Freq. Control **33**, 319–329 (1986).
[5] M. F. Insana, J. G. Wood, and T. J. Hall, ''Identifying acoustic scattering sources in normal renal parenchyma in vivo by varying arterial and ureteral pressures,'' Ultrasound Med. Biol. **17**, 613–626 (1991).
[6] E. J. Feleppa, F. L. Lizzi, D. J. Coleman, and M. M. Yaremko, ''Diagnostics spectrum analysis in ophthalmology: A physical perspective,'' Ultrasound Med. Biol. **12**, 623–631 (1986).
[7] K. C. Balaji, W. R. Fair, E. J. Feleppa, C. R. Porter, H. Tsai, T. Liu, A. Kalisz, S. Urban, and J. Gillespie, ''Role of advanced 2 and 3-dimensional ultrasound for detecting prostate cancer,'' J. Urol. (Baltimore) **168**, 2422–2425 (2002).
[8] E. Feleppa, A. Kalisz, J. Sokil-Melgar, F. L. Lizzi, L. Tian, A. L. Rosado, M. C. Shao, W. R. Fair, W. Yu, M. S. Cookson, V. E. Reuter, and W. D. W. Heston, ''Typing prostate tissue by ultrasonic spectrum analysis,'' IEEE Trans. Ultrason. Ferroelectr. Freq. Control **43**, 609–619 (1996).
[9] B. S. Garra, M. F. Insana, I. A. Sesterhenn, T. J. Hall, R. F. Wagner, C. Rotellar, J. Winchester, and R. K. Zeman, ''Quantitative ultrasonic detection of parenchymal structural change in diffuse renal disease,'' Invest. Radiol. **29**, 134–140 (1994).
[10] M. F. Insana and T. J. Hall, ''Parametric ultrasound imaging from backscatter coefficient measurements: Image formation and interpretation,'' Ultrason. Imaging **12**, 245–267 (1990).
[11] T. J. Hall, M. F. Insana, L. A. Harrison, and G. G. Cox, ''Ultrasonic measurement of glomerular diameters in normal adult humans,'' Ultrasound Med. Biol. **22**, 987–997 (1996).
[12] M. F. Insana, T. J. Hall, J. G. Wood, and Z. Y. Yan, ''Renal ultrasound using parametric imaging technique to detect changes in microstructure and function,'' Invest. Radiol. **28**, 720–725 (1993).
[13] M. L. Oelze, J. F. Zachary, and W. D. O'Brien, Jr., ''Parametric imaging of solid tumors using average scatterer size and acoustic concentration,'' 2003 World Congress on Ultrasound.
[14] M. L. Oelze, J. F. Zachary, and W. D. O'Brien, Jr., ''Differentiation of tumors types in vivo by scatterer property estimates and parametric images using ultrasound backscatter,'' Proceedings of the 2003 IEEE Ultrasonics Symposium, pp. 1022–1025.
[15] M. L. Oelze, W. D. O'Brien, Jr., and J. F. Zachary, ''Differentiation and characterization of rat mammary fibroadenomas and 4t1 mouse carcinomas using quantitative ultrasound imaging,'' IEEE Trans. Med. Imaging **23**, 764–771 (2004).
[16] M. L. Oelze, J. F. Zachary, and W. D. O'Brien, Jr., ''Parametric imaging of rat mammary tumors in vivo for the purposes of tissue characterization,'' J. Ultrasound Med. **21**, 1201–1210 (2002).
[17] F. Padilla, F. Peyrin, and P. Laugier, ''Prediction of backscatter coefficient in trabecular bones using a numerical model of three-dimensional microstructure,'' J. Acoust. Soc. Am. **113**, 1122–1129 (2003).
[18] P. M. Morse and K. U. Ingard, *Theoretical Acoustics* (McGraw-Hill, New York, 1968).
[19] K. K. Shung and G. A. Thieme, *Ultrasonic Scattering in Biological Tissues* (CRC Press, Boca Raton, FL, 1993).
[20] A. V. Oppemheim, R. W. Schaffer, and J. R. Buck, *Discrete-time Signal Processing* (Prentice Hall, Upper Saddle River, NJ, 1999).
[21] M. L. Oelze, J. F. Zachary, and W. D. O'Brien, Jr., ''Characterization of tissue microstructure using ultrasonic backscatter: Theory and technique for optimization using a Gaussian form factor,'' J. Acoust. Soc. Am. **112**, 1202–1211 (2002).
[22] J. J. Faran, ''Sound scattering by solid cylinders and spheres,'' J. Acoust. Soc. Am. **23**, 405–418 (1951).
[23] S. A. Goss, R. L. Johnston, and F. Dunn, ''Comprehensive compilation of empirical ultrasonic properties of mammalian tissues,'' J. Acoust. Soc. Am. **64**, 423–457 (1978).
[24] S. A. Goss, R. L. Johnston, and F. Dunn, ''Comprehensive compilation of empirical ultrasonic properties of mammalian tissues ii,'' J. Acoust. Soc. Am. **68**, 93–108 (1980).
[25] F. A. Duck, *Physical Properties of Tissue. A Comprehensive Reference Book* (Academic, New York, 1990).
[26] Y. Miyazaky, ''Light scattering of laser beams by random microinhomogeneities in glasses and polymer,'' Jpn. J. Appl. Phys. **13**, 1238–1248 (1974).
[27] P. A. Egelstaff, C. Gubbins, and K. C. Mo, ''Theory of inelastic neutron scattering from molecular fluids,'' J. Stat. Phys. **13**, 315–330 (1975).
[28] D. K. Wilson, J. G. Brasseur, and K. E. Gilbert, ''Acoustic scattering and the spectrum of atmospheric turbulence,'' J. Acoust. Soc. Am. **105**, 30–34 (1999).
[29] K. A. Topp, J. F. Zachary, and W. D. O'Brien, Jr., ''Quantifying b-mode images of in vivo rat mammary tumor with frequency dependence of backscatter,'' J. Ultrasound Med. **20**, 605–612 (2001).
[30] E. L. Madsen, M. F. Insana, and J. A. Zagzebski, ''Method of data reduction for accurate determination of acoustic backscatter coefficients,'' J. Acoust. Soc. Am. **76**, 913–923 (1984).
[31] M. L. Oelze and W. D. O'Brien, Jr., ''Frequency-dependent attenuation-compensation functions for ultrasonic signals backscattered from random media,'' J. Acoust. Soc. Am. **111**, 2308–2319 (2002).